# Analyst

Accepted Manuscript


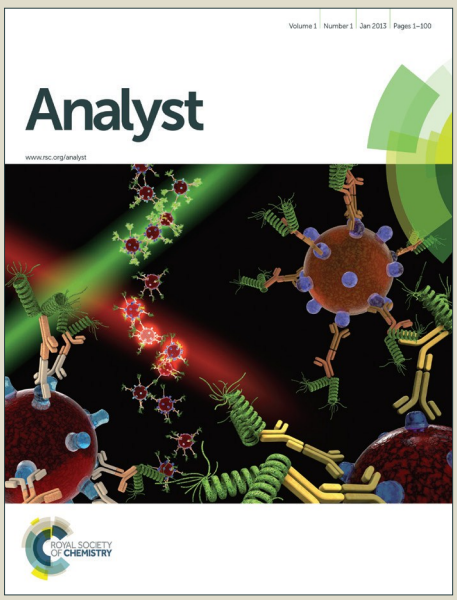





ROYAL SOCIETY OF CHEMISTRY

www.rsc.org/analyst

Analyst

ARTICLE

# Visualization of biosensors using enhanced surface plasmon resonances in capped silver nanostructures

Received 30th October 2015,
Accepted 00th January 20xx

DOI: 10.1039/x0xx00000x

www.rsc.org/

Kuang-Li Lee,[a] Meng-Lin You,[b] Cheng-Lin Tsai,[b] Chia-Yu Hung,[c] Shu-Yi Hsieh[a] and Pei-Kuen Wei[a,b,d]*

We propose a method and optical design for directly visualization of the label-free detection. The system, similar to a tiny spectral analyzer, is composed of a nanostructure-based surface plasmon resonance chip, linear polarizer and 532-nm laser light source. The full-width-at-half-maximum bandwidths of the enhanced surface plasmon resonances are about 5 nm. The distribution of the transmitted light from these arrays comprises a spectral image on the chip. The qualitative and quantitative analyses of the analyte can be conducted by observing the spot shift on the chip. We test the sensing capability of the chip. The detectable surface mass density with naked eyes is about 0.476 μg/cm$^2$. In addition, antigen-antibody interaction experiments are conducted to verify the surface binding measurements. A monolayer protein attached on the chip can be directly observed and the concentration levels of the analyte can be estimated with naked eyes. Such plasmonic bioschips can benefit sensing applications on point-of-care diagnostics.

## 1 Introduction

Surface plasmon resonance (SPR) sensing is a real-time and label-free detection technique which has been employed in applications including medical diagnostics, environmental monitoring, and food safety.[1-4] Commercial sensing platforms utilize an optical prism to induce propagating surface plasmon polaritons in thin noble films and enable real-time and label-free measurements of biomolecular binding affinity. In addition to the prism coupling method, metallic nanostructures offer a simpler way for SPR excitation.[5-9] Periodic metallic nanohole arrays or nanoslit arrays have been utilized for biosensing applications.[10-17] However, the majority of SPR sensing is performed on dedicated and expensive instruments. It would be desirable to develop a simple and inexpensive SPR system which can be utilized for point-of-care diagnostics. The colorimetric detection scheme based on plasmonic resonance phenomenon provides one possibility. Plasmonic nanoparticles (NPs) play an important role in the colorimetric detection. The color changes caused by the capture of the analyte labelled with gold NPs or the aggregation of gold NPs triggered by the bio-recognition events can be directly observed with naked eyes.[18,19] Such detection scheme is widely applied to the lateral-flow immunochromatographic assay or lateral-flow assay for single use and qualitative point-of-care test.[20,21] The commercially available product is for pregnancy confirmation and the production of the pregnancy test is more than $10^7$ per year. Different from the sandwich-type colorimetric detection with gold NPs, a simple label-free detection technique using Fano resonances in metallic nanohole arrays was proposed by Yanik et al.[22] A monolayer of biomelocule can be detected with naked eyes. The system consists of a white light source, narrow bandpass filter and nanohole-based biochips. No other expensive instruments are required. When biomolecules adsorb on the structure surface, there is an intensity change near the resonant wavelength. Such intensity change can be directly observed with naked eyes. However, the simple intensity measurement is susceptible to environmental conditions. It has a low dynamic range and cannot quantitatively determine the analyte concentration.

In this study, we proposed a method and optical design for direct visualization of the label-free detection. The system, similar to a tiny spectral analyzer, is composed of a nanostructure-based surface plasmon resonance (SPR) chip, linear polarizer and 532-nm laser light source as shown in Fig. 1(a). The plasmonic biochip consists of several capped nanoslit arrays with different periods. The capped nanoslit arrays have enhanced Fano resonances generated by the couplings of a broadband resonance and a narrowband resonance.[23,24] Compared to other resonant systems, the Fano resonance has a narrower bandwidth and higher intensity sensitivity. Our detection scheme utilizes capped silver nanoslit arrays with several different Fano resonant peaks and a laser light source. The distribution of the transmitted light from these arrays comprises a spectral image on the chip. The x-axis is the period and the y-axis is the transmitted intensity as shown in Fig. 1(b). When biomolecules adsorb on the surface of the chip, the spectral image composed of several arrays is redshifted.

[a] Research Center for Applied Sciences, Academia Sinica, Taipei 11529, Taiwan
E-mail: pkwei@sinica.edu.tw
[b] Institute of Biophotonics, National Yang-Ming University, Taipei 11221, Taiwan
[c] Department of Mechanical Engineering, National Taiwan University, Taipei 10617, Taiwan
[d] Department of Optoelectronics, National Taiwan Ocean University, Keelung 20224, Taiwan

Consequently, dramatic reductions or increases in the transmitted light intensity for different arrays are observed (See Fig. 1(c)). The qualitative and quantitative analyses of the analyte can be conducted by observing the spot shift on the chip.

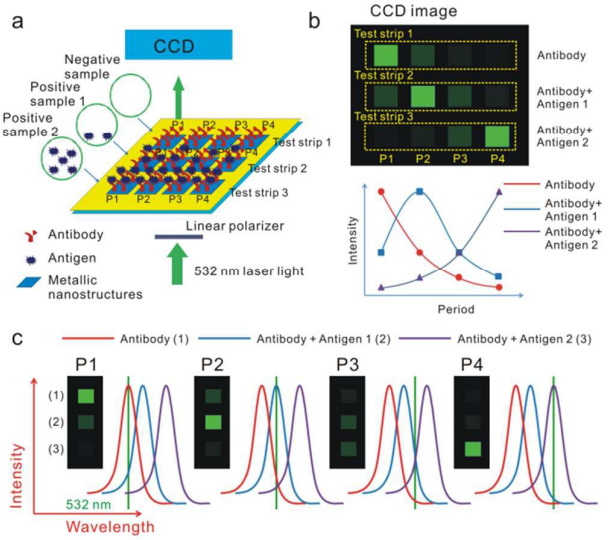


**Fig. 1** Detection scheme utilizes capped silver nanoslit biochips and a laser light source. (a) Schematic configuration of the optical system for the spectral image measurement. There were three test strips on the chip. (b) Schematic representation of the transmitted light image of the biochip and the intensity spectral for different tested samples. The brightest zone shifted with the increase of the concentration of the sample. (c) A schematic illustration depicts the relative positions of resonant wavelengths of the arrays with different periods and the wavelength of laser light. When biomolecules adsorb on the surface of the chip, it causes the redshift of the plasmonic resonances. Consequently, dramatic reductions or increases in the transmitted light intensity for different arrays are observed.

## 2 Methodology

### 2.1 Fabrication of plasmonic biochips

Fig. 2(a) shows the flow chart of the fabrication of capped metallic nanoslits. The structure consists of upper layer of periodic metallic nanowires and lower layer of periodic metallic nanoslits. The periods of both layers are the same. The biochip was made on a cyclic olefin polymer (COP) substrate using hot embossing nanoimprint lithography. First, nanogrooves of 60 nm in width and 80 nm in depth on a silicon substrate were fabricated using electron beam lithography and a reactive ion etching method. A 300-nm-thick ZEP-520 resist (ZEP-520, Zeon Corp, Tokyo, Japan) was spin-coated on a 525-μm-thick silicon substrate. An electron-beam writing system (Elionix ELS 7000) was used to write groove arrays with different groove periods. The patterns were then transferred to the silicon substrate by using a reactive ion etching machine (Oxford Instrument, plasmalab 80plus). The power of the radio frequency (RF) electromagnetic wave in the reaction chamber was 150 W. The chamber pressure was $1\times10^{-2}$ torr and the flow rates of CHF3 and SF6 gases were 50 sccm and 25 sccm, respectively. The resist was removed by rinsing the sample in acetone for a few minutes. Then, it was put in ultrapure water and purged dry by nitrogen. The substrate was a 178-μm-thick COP film. The silicon template and COP substrate were placed on a heating plate. They were heated at a temperature of 170 $^{o}$C to soften the COP substrate. In the system, nitrogen gas was introduced into the chamber to produce a pressing pressure (20 kgw/cm$^2$) over the film. An additional polyethylene terephthalate (PET) thin film was used as the sealing film. It pressed the silicon mold and COP substrate with large-area uniformity. This step made the structure uniformly stuck to the softened COP film. The template and substrate were then cooled and taken out from the chamber. After peeling off from the template and sealing film, the periodic COP ridges were made. After sputtering an 80-nm-thick silver film on the imprinted plastic substrate, the plasmonic biochip consisted of capped silver nanostructures with different periods was made. In this study, the periods of the nanostructures ranged from 471 to 650 nm. The difference of the periods between adjacent periodic nanostructures was about 1 or 3 nm. The area of each periodic nanostructure was 150×150 μm$^2$. Fig. 2(b) shows the optical image of the fabricated biochip. The transmitted light image of the biochip using white light was shown in Fig. 2(b) inset. The periods ranged from 516 to 525 nm. The difference of the periods was 1 nm. Fig. 2(c) shows a scanning electron microscope (SEM) image of the nanostructure with a period of 516 nm. The wire width was 80 nm.

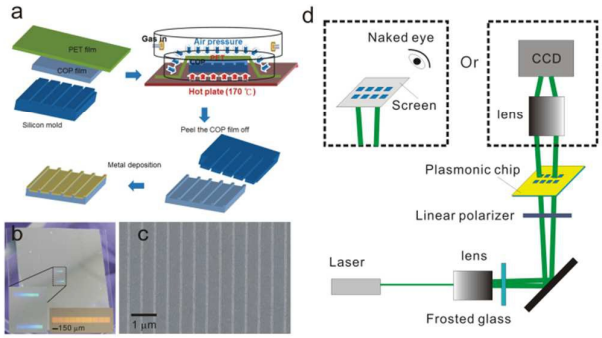


**Fig. 2** Fabrication of the capped silver nanoslit biochips and optical setup for recording spectral images. (a) The flow chart of the fabrication of capped silver nanoslits. (b) Optical image of the plasmonic biochip. The inset shows the transmitted light image of the biochip using white light. The period of the nanostructure ranged from 516 to 525 nm. (c) The scanning electron microscope image of the nanostructure with a period of 516 nm. (d) The optical setup for recording transmitted light images of the biochips.

### 2.2 Atomic layer deposition of aluminum oxide

An aluminum oxide film was deposited on the biochips using an atomic layer deposition machine (ALD, Syskey Technology CO., LTD). For deposition of aluminum oxide, the precursors of trimethylaluminum (TMA) and water were used. The chamber

working pressure was $1.2\times10^{-1}$ torr and the substrate temperature was kept at 120 °C.

**2.3 Optical setup for transmission spectrum measurements**

The transmission spectra were measured by a simple optical transmission setup.[16] A 12W halogen light was spatially filtered by using an iris diaphragm and a collimation lens. Its incident polarization was controlled by a linear polarizer. The white light was focused on a single array by using a 4× objective lens. The transmission light was collected by another 10× objective lens and focused on a fiber cable. The transmission spectrum was taken by using a fiber-coupled linear charge-coupled device (CCD) array spectrometer (BWTEK, BTC112E).

**2.4 Optical setup for recording spectral images**

Fig. 2(d) shows the optical setup for recording transmitted light images of the biochips. A 532-nm laser diode was used as a light source. The laser beam was expanded by a 10× objective lens and passed through a frosted glass to destruct the coherence. Its incident polarization was controlled by a linear polarizer. The polarized light was normally incident on the biochip and the polarization was perpendicular to the nanoslits. The transmitted light was then collected by a 4× objective lens and recorded by a CCD. It is noted that the spectral image on the chip can be observed with naked eyes.

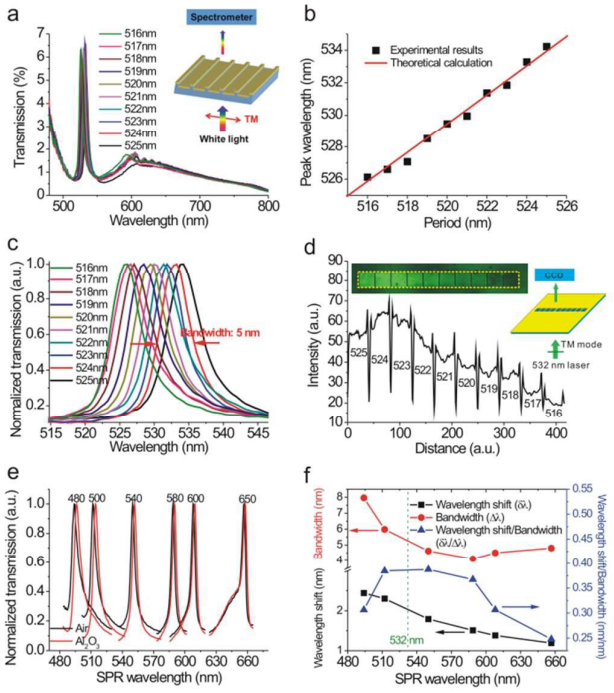


**Fig. 3** Optical properties of the capped silver nanoslit biochips. (a) The measured transmission spectra of the capped silver nanoslits with different periods in air for normally-incident TM-polarized light. The periods were from 516 to 525 nm. The difference of the periods was 1 nm. (b) Experimental peak wavelengths of SPR resonances and theoretical (equation 2) resonant wavelengths of BW-SPPs as a function of the period. (c) Normalized transmission spectra of the capped metallic nanoslits with different periods. The FWHM bandwidth was about 5 nm. (d) The intensity distribution of the transmitted light image indicated with dashed line in the inset. The inset shows the transmitted light image of the biochip using 532-nm laser light. (e) Normalized spectra of the nanostructures with different periods before and after coating a thin $Al_2O_3$ film on the chip for normally-incident polarized light. The period ranged from 480 to 650 nm. (f) The wavelength shift, bandwidth and ratio (wavelength shift/bandwidth) as a function of the SPR wavelength. The wavelength shift caused by the thin film and the bandwidth were increased with the decrease of the resonant wavelength. It results in an optimal ratio between the wavelength shift and bandwidth near the wavelength of 532 nm.

## 3 Results and Discussion

**3.1 Optical properties of the capped silver nanoslit biochips**

The key element of the chip was the periodic capped silver nanoslits. It consisted of upper layer of periodic silver nanowires and lower layer of periodic silver nanoslits. The periods of both layers were the same. We fabricated an array of the capped silver nanostructures with different periods. The period ranged from 516 to 525 nm. The difference of the periods between adjacent periodic nanostructures was about 1 nm. Fig. 3(a) shows the measured transmission spectra of the plasmonic biochip in air for normally-incident polarized light. The polarization of the incident light was perpendicular to the nanoslits because the gap plasmons in nanoslits and surface plasmons on the periodic surface can only be excited by using transverse magnetic (TM)-polarized incident light. There were two resonant modes in the spectra. One was the gap plasmon resonances (cavity mode) and the other Bloch wave surface plasmon polaritons (BW-SPPs) on the periodic metal surface. The cavity mode occurred within the nanoslit which generates a broadband resonance in the transmission spectrum. The resonant condition can be estimated by the Fabry-Perot cavity,[25]

$$2n_{eff}k_0h+\phi_1+\phi_2=2m\pi \qquad (1)$$

where $n_{eff}$ is the equivalent refractive index in the slit, $k_0$ is the free space wavelength vector $(2\pi/\lambda_0)$, $h$ is the height of the periodic ridge, and $\phi_1$ and $\phi_2$ are the phase shifts at the top and bottom interfaces. The resonant wavelength is affected by the slit width and height. The resonant wavelength of the cavity mode was around 600 nm and was independent of the period. On the other hand, the BW-SPP occurs on the periodic nanoslits when the Bragg condition is satisfied. It generates a narrowband transmission in the measured spectrum. For normally incident light, the condition for a 1-D array can be described by,

$$\lambda_{SPR}(n,i)=\frac{P}{i}\mathrm{Re}\{(\frac{\varepsilon_m n^2}{\varepsilon_m+n^2})^{1/2}\} \qquad (2)$$

where $i$ is the resonant order, $P$ is the period of the nanostructure, $\varepsilon_m$ is the dielectric constant of the metal and $n$ is the environmental refractive index. The resonant wavelength of the BW-SPP is in proportion to the period. The cavity mode had an overlap with the BW-SPP mode. The coupling of the broadband cavity mode to the narrowband BW-SPP mode generated a sharp Fano resonance. The Fano resonant wavelength occurred near the $\lambda_{SPR}$. Fig. 3(b) shows the experimental Fano resonant wavelengths were proportional to

the periods and close to the calculated values by equation (2). The second layer, periodic nanowires on the top surface, provided an enhanced confinement for surface plasmon resonances as compared to the single-layer nanoslit array.[26] Such an enhanced surface plasmon mode greatly increased the resonant quality of the Fano resonance. It was noted that the capped gold nanoslit array was proposed in our previous study.[26] However, the interband transition for a gold film is around 550 nm. In order to match with the green light source, the gold film was replaced by a silver film. In the experiment, the full width at half maximum (FWHM) bandwidth of the enhanced SPR resonance was about 5 nm (see Fig. 3(c)). The enhanced SPR in capped metallic nanostructures can fulfill the requirement of the narrow resonant bandwidth. Figure 3(d) inset shows the transmitted light image of the biochip using 532-nm laser light. The distribution of the transmitted light from these arrays formed a spectral image on the chip. The x-axis was the period and the y-axis was the transmission intensity, as shown in Fig. 3(d). Fig. 3(e) shows that normalized spectra of SPR modes of the nanostructures with different periods before and after coating a dielectric thin film, aluminum oxide ($Al_2O_3$), on the chip. The $Al_2O_3$ film was coated by the ALD method and the nanoslit period ranged from 480 to 650 nm. Obviously, the wavelength shift caused by the thin film and the bandwidth were increased with the decrease of the resonant wavelength as shown in Fig. 3(f). It results in an optimal ratio between the wavelength shift and bandwidth near the wavelength of 532 nm (see Fig. 3(f)). Therefore, the 532-nm laser light was utilized in this study.

### 3.2 Surface sensing capabilities of the capped silver nanoslit biochips

As the minimum detectable surface mass density is a value to evaluate the quality (or sensitivity) of a sensor, the surface sensitivity of the biochip was tested by coating three different thicknesses of $Al_2O_3$ films on the chip. Fig. 4(a) shows the schematic representation of transmitted light images for $Al_2O_3$ thicknesses ranged from 0 to 8.9 nm. The deposited $Al_2O_3$ film resulted in reductions or increases in the transmitted light intensity for different periodic nanostructures. With the increase of the film thickness, the brightest zone was moved from the 523-nm-period nanostructure to 516-nm-period nanostructure as shown in Figure 4(b). Fig. 4(c) shows the intensity distribution of the spectral image for different film thicknesses. The brightest zone shifted to right with the increase of the film thickness. There was a linear correlation between the brightest zone shift (#) and film thickness, as shown in the inset of Fig. 4(c). The slop was 0.785 #/nm. It means that a 1.27-nm $Al_2O_3$ film resulted in one block shift. Because the density of aluminum oxide is 3.75 g/cm$^3$, the detectable surface mass density with naked eyes is about 0.476 μg/cm$^2$. To compare the results with conventional measurements using a spectrometer, we also measured transmission spectra of the capped nanostructures. Fig. 4(d) shows the spectra with periods of 516 and 525 nm for different film thicknesses. The resonant peak was redshifted with the increase of the film thickness. There were linear correlations between the peak shift and the film thickness. The slopes or wavelength sensitivities were 0.64 and 0.59 nm/nm for 516-nm-period and 525-nm-period array, respectively (see Fig. 4(d) inset). The averaged spectral sensitivity was about 0.6 nm/nm. It means that a 1.27-nm-thick $Al_2O_3$ film results in a wavelength shift of 0.762 nm. As the peak wavelength difference between the 523-nm-period and 522-nm-period arrays is 0.47 nm, the brightest zone was moved from the 523-nm-period array to 522-nm-period array as shown in Fig. 4(b) and Fig. 4(c). Therefore, the unknown film thickness can be directly estimated by observing the movement of the brightest zone in the image. The qualitative and quantitative analyses for measuring the film thickness can be achieved without using the expensive spectrometer. In addition, the dynamic range or the range of film thickness measurements for the proposed method is tuneable by changing the array number and period difference between adjacent arrays. It was noted that the figure of merit (FOM) is usually defined as $S_\lambda$/bandwidth, where $S_\lambda$ is the wavelength sensitivity which is similar to the period.[16] In our sensing chip for 520-nm period, the FOM is ~491/5.0= 98. This value is comparable to the theoretically estimated upper limits (FOM=108) of the prism-coupling SPR sensors[27] and the FOM value (108) of gold mushroom arrays.[28] The limit of detection (LOD) is dependent on the resolution of the detection method. In our chip, the periodic difference between two neighboring blocks is 2 nm. It results in a LOD of 0.476 μg/cm2. This surface mass density is smaller than prism-based SPR sensing technique with dedicated and expensive instruments. However, with a lower SPR bandwidth and a smaller periodic difference, the LOD can be further improved.

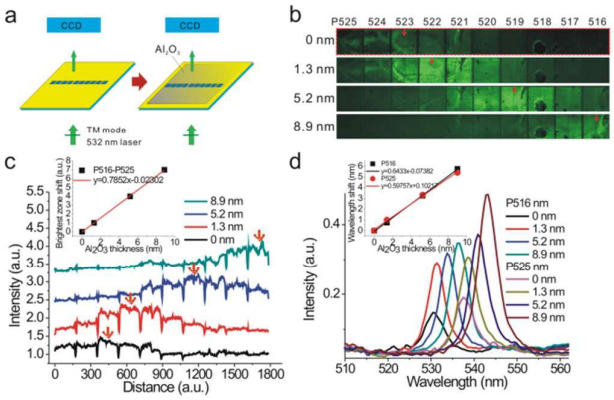


**Fig. 4** Surface sensing capabilities of the capped silver nanoslit biochips. (a) The schematic representation of recording transmitted light images of biochips encapsulated with an ALD-grown $Al_2O_3$ film. (b) Spectral images of the chip for different thicknesses of the $Al_2O_3$ films. The brightest zone was moved with the increase of the film thickness. (c) The intensity distributions of the spectral images indicated with dashed line in panel b for different film thicknesses. The inset shows the brightest zone shift against the film thickness. (d) The transmission spectra of the capped nanosilts with periods of 516 and 525 nm for different film thicknesses. The inset shows the peak wavelength shift against the film thickness for different periodic nanostructures. There was a linear correlation between the peak shift and film thickness. The wavelength/thickness sensitivity was about 0.6 nm/nm.

### 3.3 Biosensing using the capped silver nanoslit biochips

We further conducted protein-protein specific interaction experiments using the plasmonic biochips. Anti-proteins such as anti-bovine serum albumin (anti-BSA, Sigma-Aldrich) and anti-penicillin-binding proteins (anti-PBP2α, Abcam) were chosen for the

binding and nonbinding experiments. The plasmonic biochip consisted of 19 capped silver nanoslits with different periods. The period ranged from 471 to 525 nm. The difference of the periods between adjacent arrays was about 3 nm. The transmitted light images of the chip for different surface conditions were subsequently recorded by a CCD. Fig. 5(a) shows the experimental flow chart of the antigen-antibody interaction. First, the plasmonic biochip was encapsulated with a 4-nm-thick $Al_2O_3$ shell to protect the patterned Ag from oxidation. This method has been proposed by some other groups.[29,30] The protected sample is stable for at least 9 months.[29] The chip was then exposed to a 95% ethanol at room temperature for 5 minutes and purged dry by nitrogen gas. In order to immobilize bovine serum albumin (BSA, Sigma-Aldrich) on the structure surface, the biochips with a 4-nm-thick $Al_2O_3$ shell was exposed to a 10% aminopropyltriethoxysilane (APTES) solution for 30 minutes and then baked at 120 $^{o}$C for 1 hour to form amino groups on the $Al_2O_3$ film surface. After modification of the amino groups, a 20 µL of 1mg/mL Bovine serum albumin (BSA, Sigma-Aldrich) solution was dropped on the structure surface for 1 hour. The sample was then washed by ultrapure water to remove the unbound BSA proteins and purged dry by nitrogen gas.

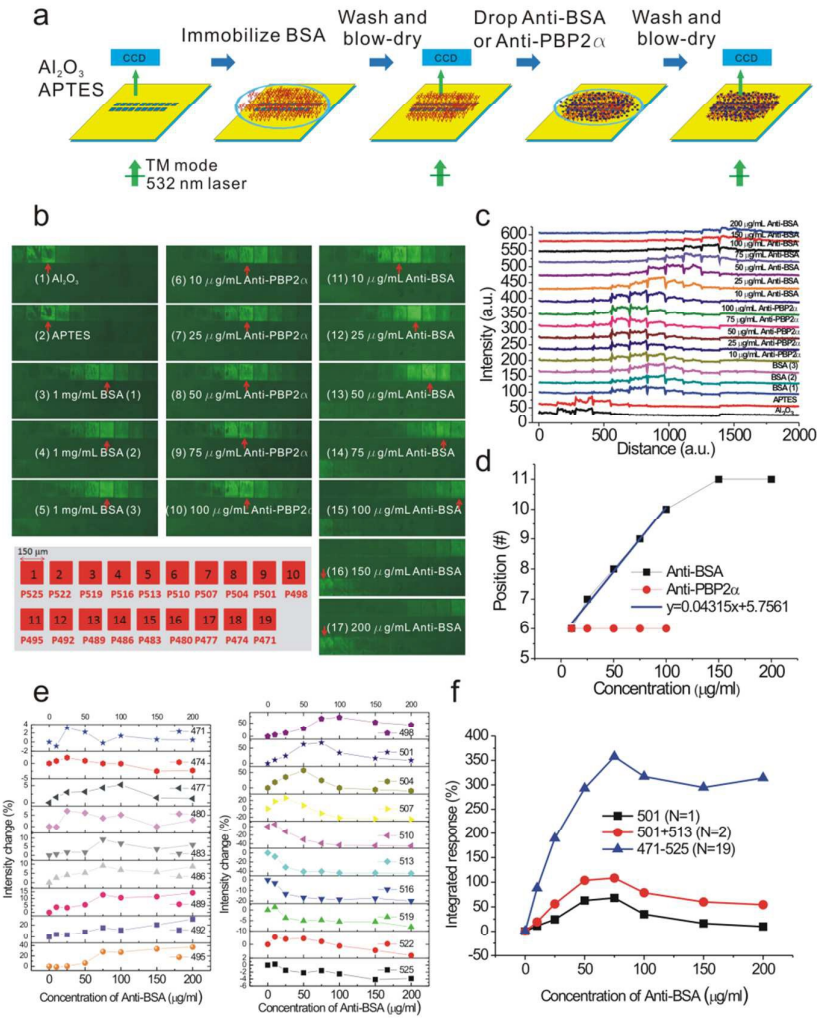


**Fig. 5** Biosensing using the capped silver nanoslit biochips. (a) The experimental flow chart of the antigen-antibody interactions. (b) The spectral images of the chip for different surface conditions. The chose period of the capped nanoslits ranged from 471 to 525 nm. The difference of the periods was 3 nm. (c) The intensity distributions of the spectral images in panel b for different surface conditions. (d) The position of the brightest zone of the spectral image as a function of the concentration of the tested sample (anti-BSA and anti-PBP2α). The position of the brightest spot remained unchanged for different anti-PBP2α solutions. There was a linear correlation between the spot position and the concentration of the anti-BSA solution. The slop was 0.043 #/µg/mL. The 23.20 µg/ml anti-BSA solution results in one block shift. (e) The intensity changes as a function of the Anti-BSA concentration for all arrays on the chip. The highest intensity sensitivity was 1.25 %/(µg/mL) for the 501-nm-period array. (f) The integrated response as a function of the Anti-BSA concentration. The integrated response shows a six times improvement when the array number was increased from 1 to 19.

In order to make sure that sufficient BSA was immobilized on the structure surface, the BSA coating process was repeated for three times. Next, nonbinding anti-PBP2α proteins with various concentrations were detected. A 10 µL of 10 µg/mL anti-PBP2α solution was dropped on the structure surface for 30 minutes. The sample was then washed by ultrapure water and purged dry by nitrogen gas. The dropping, washing and nitrogen-purged dry processes were subsequently repeated for various concentrations of anti-PBP2α solutions from 10 to 100 µg/mL. Finally, specific binding anti-BSA samples with various concentrations from 10 to 200 µg/mL were tested. The processes such as anti-BSA binding, washing and nitrogen-purged dry were subsequently repeated for many times. Fig. 5(b) shows the transmitted images of the chip for different surface conditions. Fig. 5(c) shows the intensity distributions of the spectral images in Fig. 5(b) for different surface conditions. At first, the brightest zone located at 522-nm-period nanostructure (Zone 3) when the biochip was encapsulated with a 4-nm-thick Al2O3 shell. After the modification of amino groups using APTES, dramatic intensity reduction for 522-nm-period nanostructure (Zone 2) and intensity increase for 516-nm-period nanostructure (Zone 4) are observed. The brightest zone was still at 522-nm-period nanostructure (Zone 3). Next, when the monolayer BSA adsorbed on the structure surface, the brightest zone shifted 4 blocks (Zone 7). The position of the brightest zone remained unchanged (Zone 7) after the BSA coating process was repeated for three times. After detecting 10 mL of 10 µg/mL anti-PBP2α solution, we found that the brightest zone shifted to left (Zone 6). We deduced that the concentration of the BSA solution may be too high. Some BSA proteins detached from the surface when anti-PBP2α proteins were added. After conducting unbinding experiments with various concentrations of anti-PBP2α solutions from 10 to 100 µg/mL, we found that the position of the brightest zone remained unchanged (Zone 7). On the other hand, the brightest zone shifted 5 blocks and then kept unchanged when the concentration of the anti-BSA solution was increased from 10 to 200 µg/mL. The above results indicate that the interaction between BSA and anti-BSA is highly specific. Fig. 5(d) shows the position of the brightest zone of the spectral image as a function of the concentration of the tested sample (anti-BSA and anti-PBP2α solutions). The position of the brightest spot remains unchanged for different anti-PBP2α solutions. However, there was a linear correlation between the spot position and the concentration of the anti-BSA solution. The slop was 0.043 #/µg/mL. It indicates that 23.20 µg/ml anti-BSA solution results in one block shift. Compared to the intensity measurement using single metallic nanohole array, the proposed method measures the spectral shift of the spectral image and has a wider dynamic (or operating) range. In addition, the spectral images can be analyzed with a spectral integration method, which can increase the signal-to-noise ratio of the system and effectively improve the sensing capability.[31,32] Fig. 5(e) shows the intensity changes as a function of the Anti-BSA concentration for all arrays on the chip. There was a linear correlation between the intensity change and concentration when the Anti-BSA concentration was below 50 µg/mL. The highest intensity sensitivity was 1.25 %/(µg/mL) for the 501-nm-period array. We further analyzed the data with the spectral integration method. The integrated response (R) is defined by the absolute value of the difference of the normalized transmission spectra:

$$R(h) = \sum_{n=1}^{N} \left| \frac{I(h,n) - I(h_0,n)}{I(h_0,n)} \times 100\% \right| \qquad (3)$$

where the *I(h, n)* is transmitted intensity under different Anti-BSA concentration, *h* is the test sample, $h_0$ is the reference sample and *N* is the number of metallic nanostructures. By utilizing equation (3), setting the spectral image of the 0 µg/mL anti-BSA sample as a reference and choosing the number of metallic nanostructures (N=1, 2 and 19), the integrated response as a function of the Anti-BSA concentration was shown in Fig. 5(f). Obviously, there was a correlation between the integrated response and Anti-BSA concentration below 50 µg/mL. The integrated response shows a six-time improvement when the array number was increased from 1 to 19. Therefore, the proposed method can further improve the sensing capability with the spectral integration method.

## Conclusions

We demonstrated an easy, low-cost and label-free technique for qualitative and quantitative detection of specific bio-interactions. No other expensive instruments are required. The concentration levels of the analyte can be directly estimated with naked eyes. Once various recognition molecules are immobilized on the chip, it can be utilized to detect multiple analytes. Compared to the lateral-flow assay, the proposed method is a label-free detection technique and can be applied to qualitative and quantitative chip-based high-throughput detection. Compared to the label-free detection technique using single metallic nanohole array, which only measured the intensity change at a certain wavelength, the proposed method measures the spectral shift of the spectral image. It is more reliable and can avoid the problem of intensity fluctuations. The spectral image measurement also takes the advantage of a larger dynamic range. In addition, the spectral image can be analyzed by a spectral integration method, which can increase the signal-to-noise ratio of the system and effectively improve the sensing capability. The proposed nanostructures and measurement setup can provide a good feasibility for point-of-care diagnostics.

## Acknowledgements

This work was supported by National Science Council, Taipei, Taiwan, under Contract no. MOST 103-2221-E-001-013-MY3 and MOST 104-2112-M-001-040-MY2 and by the Bureau of Animal and Plant Health Inspection and Quarantine of Taiwan, under Contract no. 104AS-15.3.1-BQ-B1. Technical support from the core facilities for nanoscience and nanotechnology and the scientific instrument facility at Institute of Chemistry, Academia Sinica in Taiwan, is acknowledged.

## References


1 H. Raether, Surface plasmons on smooth and rough surfaces and on gratings, Springer-Verlag, Berlin, Heidelberg, 1988.
2 J. Homola, S. S. Yee and G. Gauglitz, *Sens. Actuator B: Chem.*, 1999, **54**, 3-15.
3 S. A. Maier, Plasmonics: Fundamentals and Applications, Springer Science, New York 2007, 188-192.
4 J. Homola, *Chem. Rev.*, 2008, **108**, 462-493.
5 T. W. Ebbesen, H. J. Lezec, H. F. Ghaemi, T. Thio and P. A. Wolff, *Nature*, 1998, **391**, 667-669.
6 S. Kawata, Near-Field Optics and the Surface Plasmon Polariton, Springer-Verlag, New York, 2001, Ch. 1.
7 H. J. Lezec, A. Degiron, E. Devaux, R. A. Linke, L. Martin-Moreno, F. J. Garcia-Vidal and T. W. Ebbesen, *Science*, 2002, **297**, 820-822.
8 M. E. Stewart, C. R. Anderton, L. B. Thompson, J. Maria, S. K. Gray, J. A. Rogers and R. G. Nuzzo, *Chem. Rev.*, 2008, **108**, 494-521.
9 J. N. Anker, W. P. Hall, O. Lyandres, N. C. Shah, J. Zhao and R. P. Van Duyne, *Nat. Mater.*, 2008, **7**, 442-453.
10 A. G. Brolo, R. Gordon, B. Leathem and K. L. Kavanagh, *Langmuir*, 2004, **20**, 4813-4815.
11 K. A. Tetz, L. Pang and Y. Fainman, *Opt. Lett.*, 2006, **31**, 1528-1530.
12 J. Henzie, M. H. Lee and T. W. Odom, *Nat. Nanotech.*, 2007, **2**, 549-554.
13 J. C. Yang, J. Ji, J. M. Hogle and D. N. Larson, *Nano Lett.*, 2008, **8**, 2718-2724.
14 R. Gordon, D. Sinton, K. L. Kavanagh and A. G. Brolo, *Accounts Chem. Res.*, 2008, **41**, 1049-1057.
15 H. Im, S. H. Lee, N. J. Wittenberg, T. W. Johnson, N. C. Lindquist, P. Nagpal, D. J. Norris and S. H. Oh, *ACS Nano*, 2011, **5**, 6244-6253.
16 K. L. Lee, C. H. Lee, W. S. Wang and P. K. Wei, *J. Biomed. Opt.*, 2007, **12**, 044023.
17 K. L. Lee, W. S. Wang and P. K. Wei, *Biosens. Bioelectron*, 2008, **24**, 210-215.
18 T. A. Taton, C. A. Mirkin and R. L. Letsinger, *Science*, 2000, **289**, 1757-1760.
19 R. Elghanian, J. J. Storhoff, R. C. Mucic, R. L. Letsinger and C. A. Mirkin, *Science*, 1997, **277**, 1078.
20 G. A. Posthuma-Trumpie, J. Korf and A. Van Amerongen, *Anal. Bioanal. Chem.*, 2009, **393**, 569.
21 V. Gubala, L. F. Harris, A. J. Ricco, M. X. Tan and D. E. Williams, *Anal. Chem.*, 2012, **84**, 487.
22 A. A. Yanik, A. E. Cetin, M. Huang, A. Artar, S. H. Mousavi, A. Khanikaev, J. H. Connor, G. Shvets and H. Altug, *Proc. Natl. Acad. Sci. U.S.A.*, 2011, **108**, 11784.
23 A. E. Miroshnichenko, S. Flach and Y. S. Kivshar, *Rev. Mod. Phys.*, 2010, **82**, 2257-2298.
24 B. Luk'yanchuk, N. I. Zheludev, S. A. Maier, N. J. Halas, P. Nordlander, H. Giessen and C. Chong, *Nat. Mater.*, 2010, **9**, 707-715.
25 R. Gordon, *Phys. Rev. B*, 2006, **73**, 153405.
26 K. L. Lee, J. B. Huang, J. W. Chang, S. H. Wu and P. K. Wei, *Sci. Rep.*, 2015, **5**, 8547.
27 K. S. Phillips, Anal. Bioanal. Chem. 2008, **390**, 1221-1222.
28 Y. Shen, J. Zhou, T. Liu, Y. Tao, R. Jiang, M. Liu, G. Xiao, J. Zhu, Z. K. Zhou, X. Wang, C. Jin and J. Wang, *Nat. Commun.* 2013, **4**, 2381.
29 X. Zhang, J. Zhao, A. V. Whitney, J. W. Elam, R. P. Van Duyne, *J. Am. Chem. Soc.*, 2006, **128**, 10304-10309.
30 H. Im, N. C. Lindquist, A. Lesuffleur, S. H. Oh, *ACS Nano*, 2010, **4**, 947-954.
31 M. E. Stewart, N. H. Mack, V. Malyarchuk, J. A. N. T. Soares, T. W. Lee, S. K. Gary, R. G. Nuzzo and J. A. Rogers, *Proc. Natl Acad. Sci. U.S.A.*, 2006, **103**, 17143.
32 K. L. Lee, M. J. Chih, X. Shi, K. Ueno, H. Misawa and P. K. Wei, *Adv. Mater.*, 2012, **24**, OP253-OP259.